



City Research Online

City St George's, University of London

Citation: Wang, Y., Guo, L., Li, H. & Fu, F. (2022). Axial and hysteretic behavior of T-shaped steel-concrete composite shear walls. *Structures*, 38, pp. 279-291. doi: 10.1016/j.istruc.2022.01.091

This is the accepted version of the paper.

This version of the publication may differ from the final published version. To cite this item please consult the publisher's version.

Permanent repository link: <https://openaccess.city.ac.uk/id/eprint/27590/>

Link to published version: <https://doi.org/10.1016/j.istruc.2022.01.091>

Copyright and Reuse: Copyright and Moral Rights remain with the author(s) and/or copyright holders. Copies of full items can be used for personal research or study, educational, or not-for-profit purposes without prior permission or charge, unless otherwise indicated, provided that the authors, title and full bibliographic details are credited, a hyperlink and/or URL is given for the original metadata page and the content is not changed in any way. For full details of reuse please refer to [City Research Online policy](#).

Axial and hysteretic behavior of T-shaped steel-concrete composite shear walls

Yunhe Wang^{a,b}, Lanhui Guo^{a,b,*}, Hongda Li^{a,b} and Feng Fu^c

^a Key Lab of Structures Dynamic Behavior and Control of the Ministry of Education, Harbin Institute of Technology,
Harbin 150090, China

^b Key Lab of Smart Prevention and Mitigation of Civil Engineering Disasters of the Ministry of Industry and
Information Technology, Harbin Institute of Technology, Harbin 150090, China

^c School of Mathematics, Computer Science & Engineering, University of London, London, UK, EC1V0HB.

Abstract

Multi-partition steel tube formed T-shaped composite shear wall is a new type of composite wall which enhances the structural performance compared to a traditional composite shear wall. To clearly understand the behavior of such shear walls, eight half-scaled specimens were tested to study their axial and seismic behavior. The failure mechanism, structural behavior and energy dissipation ability were observed according to the experiments. The axial experiments showed that the strength of such cross-section was higher than the sum of capacities of concrete and steel tube as the multi-partition steel tube could confine the concrete well. Meanwhile, the ductility of specimens was good. For seismic experiments, the specimens exhibited high strength, good ductility and excellent energy dissipation ability. When the axial load ratio increased, the lateral load resistance capacity and energy dissipation capacity increased obviously. Although the axial load ratio was beyond the limitation of the current Chinese standard, the drift angle could still satisfy the requirement of the standard. The experimental results were used to compare with those calculated results according to some codes including EC4, CECS and AISC.

Keywords: composite shear walls; axial behavior; height-to-width ratio; seismic behavior; axial load ratio.

1. Introduction

Recently, concrete-filled steel tubes (CFSTs) were commonly applied for structural members in multistory buildings as their static and hysteretic behavior were excellent [1-3]. However, the

28 conventional square or rectangular shape corner columns in a room would reduce the actual usable
1 space for occupants and it is unaesthetic [4]. To overcome these problems, T-shaped and L-shaped
29 components are commonly applied in the structures [5]. As the special-shaped reinforced concrete
4 (RC) columns performed poor behavior under the static and hysteretic behavior [6-7], the composite
530 concept has been applied to form the special-shaped steel-concrete composite columns, improving
6 performance of special-shaped RC columns.
731

8 In recent years, T-shaped and L-shaped composite columns have been used in structures in China.
9 Some research work has been done to study the behavior of special-shaped columns [8-14]. In general,
1032 the special-shaped composite column exhibits high load resistance and good ductility if the local
11 buckling could be restrained effectively. The past research work showed that the steel plate at the
1233 convexity would buckle, as shown in Fig. 1(a). Meanwhile, if the length or depth of the cross-section
13 is large and the thickness of the steel plate is very thin, the breadth-to-thickness ratio or depth-to-
14 thickness ratio of the steel plate may be beyond the limit specified in the design code. Hence, the steel
1534 plate would buckle before yielding. Thus, the load-carrying capacity and ductility would decrease
16 obviously. To improve the local stability of the steel plate, stiffeners are necessary according to the
1735 past research work. In reality, the multi-partition cross-section is a good way to improve the stability
18 of the steel plate. The inner steel plate can connect two opposite plates instead of stiffeners and studs
1940 as illustrated in Fig. 1(b). Meanwhile, each partition works as an individual rectangular composite
20 column and its steel tube would further confine the core concrete. As a result, the capacity of load
21 resistance and ductility of multi-partition special-shaped columns would be larger than that of
22 traditional special-shaped specimens with stiffeners or studs. The special-shaped columns are
23 primarily designed to resist the axial load or eccentric load in the structures. With the increase of
24 structure height, the requirement of lateral resistance becomes higher. To improve the lateral load
25 resistance of special shaped members, it is a good way to increase the length or depth of special-
26 shaped columns. With the increase of breadth or width of the special-shaped cross-section, the depth-
27
28
29
30
31
32
33
34
35
36
37
38
39
40
41
42
43
44
45
46
47
48
49
50
51
52
53
54
55
56
57
58
59
60
61
62
63
64
65

53 to-width ratio or length-to-width ratio cross-section would be large and the special-shaped component
1
2
3
4
54 would work as the steel-concrete composite shear walls (SCCSWs).

55 A Multi-partition steel tube applied in the SCCSWs would simplify the construction progress and
6
7
8
9
10
11
12
13
14
15
16
17
18
19
20
21
22
23
24
25
26
27
28
29
30
31
32
33
34
35
36
37
38
39
40
41
42
43
44
45
46
47
48
49
50
51
52
53
54
55
56
57
58
59
60
61
62
63
64
65

enhance the stability of the steel plate during the construction stage. As shown in Fig. 1(b), this new type of multi-partition steel tube can be composited by steel pipe, H-shaped steel or steel plate. Such novel composite shear walls would work in the way of CFSTs. During construction, the inner steel plates are hardly connected at the joint of two construction parts. Commonly, the inner steel plate bears a small portion of the vertical load, as these two inner steel plates are not welded together. Thus, the inner steel plate connecting two opposite steel plates is primarily to confine core concrete, which would improve the capacity of load resistance and ductility.

Compared with the traditional components, the multi-partition composite shear wall has many advantages. Thus, it was applied in some structures in China. However, during the design, the composite action is neglected. Limitation of axial load ratio from special-shaped RC columns is used for this type of wall in the design, which would be too conservative as these improved composite shear walls behaved better than the RC column under the complex load.

Recently, some researchers made experiments for investigating the performance of such shear walls [15-20]. Zhang [15-16] studied the seismic behavior of bundled lipped channel concrete composite shear walls. In their researches, the design axial load ratio varied from 0.51 to 0.62. Thus, the axial load ratio was not very high. [Qin \[17\] proposed composite shear wall with truss connectors and studied the eccentric behavior.](#) Guo [18] made a fundamental study on the rectangular composite shear walls. The static and hysteretic behavior of composite shear walls using the multi-partition steel tube were studied. Shi [19-20] used the steel-bar space trusses to strengthen the faceplates and the concrete-filled steel tube as the boundray. The axial and seismic behavior were analyzed. From available research or literature, there was little research work on axially loaded behavior of special-shaped multi-partition composite shear walls. Thus, one task in this paper was to investigate the

78 structural performance of this new type of wall under axial load, including two loading modes. The
1
2
3 79 other aim was to investigate the seismic behavior of such shear walls under high axial load ratio. This
4
5 80 research would help understand the static and hysteretic behavior of such special-shaped composite
6
7 81 shear walls.
8
9

10 82 **2. Testing program**

11 12 83 *2.1. Test specimens*

13
14
15 84 Eight T-shaped composite shear walls were fabricated and tested. Six of them were used for axial
16
17 85 experiments. The other two of them were tested under cyclical lateral loads with constant axial loads.
18
19
20 86 The axial test is to investigate the axial strength and ductility of these composite shear walls.
21

22 87 The wall width applied in the engineering is commonly chosen as 200 mm. Considering the
23
24 88 capacity of the devices for the seismic experiments, the scale factor in the design of the specimen was
25
26
27 89 chosen as 0.5. All the specimens have the same cross-section as illustrated in Fig. 2(a). The width of
28
29 90 the specimen is 100 mm. The depth and the length of the cross-section are 300 mm and 400 mm,
30
31
32 91 respectively. For T-shaped composite shear walls, the cross-section is asymmetric about the y-axis as
33
34 92 shown in Fig. 2(a). The T-shaped cross-section develops different bending moment resistances when
35
36 93 it is subjected to the positive and negative bending moments about the neutral axis parallel with its
37
38
39 94 flange as shown in Fig. 2(a). The steel tube was composited by the 3 mm thick steel plates according
40
41 95 to the weldings. To strengthen the toe of the T-section and avoid its early failure, a 6 mm thick hot
42
43
44 96 rolled square pipe was applied.
45

46 97 During the fabrication of the multi-partition steel tube, the specimen was divided into three parts
47
48
49 98 during processing; one rolled square pipe and two welded steel sections, shown in Fig 2(b). First, the
50
51 99 welded section steels were welded by steel plates with fillet weld joints. Then, the three parts were
52
53
54 100 welded together according to the fillet weld. In reality, in the construction site, the inner steel plate
55
56 101 could not be welded together when the segments are connected in the vertical direction. The major
57
58
59 102 role of the inner steel plate is to improve the stability of the steel plate and restrain the core concrete
60
61
62
63
64
65

103 during the service stage rather than to bear the vertical load. Therefore, there was a 20 mm gap
1
2
104 between the endplate and inner plate as shown in Fig. 2(c). To satisfy the flowability of the concrete,
3
4
105 self-compacting concrete was used in the experiments.
6

7
106 In practice, for stub columns, the tested strength represents the axial capacity when the height-to-
8
9
107 width ratio of the cross section is about 3. If the height-to-width ratio were too small, the boundary
11
12
108 of the compression loading machine would influence the axial strength. If the height-to-width ratio
13
14
109 were too large, the second-order effect would reduce the capacity of load resistance. While for T-
16
17
110 shaped specimens, the breadth-to-width ratio or the depth-to-width ratio are applied to design stub
18
19
111 specimens, but there is little research work to study the influence of breadth-to-width ratio or depth-
20
21
112 to-width ratio of shear walls. Thus the height-to-width ratio is one main parameter in this research.
23
24
113 Meanwhile, the influence of loading modes on stub specimens is studied. The axial cyclic loading
25
26
114 experiments were to get the initial stiffness, reloading stiffness and unloading stiffness. Thus, the
28
29
115 hysteretic curve loading and unloading rules could be got from the axial cyclic loading experiments.
30
31
116 For the multi-partition composite shear walls subjected to the hysteretic lateral load, the sections
33
34
117 might transfer from compression to tension. The results of the axial experiments could be the
35
36
118 theoretical basis for the prediction of hysteretic curves. Two different loading modes are
37
38
119 monotonically axial compression and cyclical axial compression.
40

41
120 For the seismic tests (CSW-T-03 and CSW-T-05), the tested axial load ratio n_t , calculated by the
42
43
121 applied axial load over the axial strength, is considered as the main parameter. During calculating
45
46
122 axial strength, the strength of concrete would be higher because of the steel-concrete interaction. Thus,
47
48
123 the real strength is applied to calculate the axial load ratio for specimen subjected to cyclical lateral
50
51
124 loads. For shear walls, the design axial load ratio considering the safety factor is limited strictly in
52
53
125 Chinese code to avoid brittle failure. The design axial load ratio is calculated by the axial load over
54
55
126 the design strength of the specimen. In the calculation of design strength, the design values of material
57
58
127 are used. According to Nie's research work [21], the design axial load ratio and tested axial load ratio
59

128 are calculated and listed in Table 1. The maximum design axial load ratio in this research could be
1
2
129 0.93, which was much higher than the limitation of design guidelines [22].
3

4
130 As shown in Fig. 2, two endplates and a reinforced concrete beam were set as the boundary of the
5
6
7
131 axially loaded specimens and the seismic specimens, respectively. The dimension of the reinforced
8
9
10
132 concrete beam was shown in Fig. 2(d) - (e). In addition, some circular holes and rectangular holes
11
12
133 were cut on the multi-partition steel tube to allow the rebar to run through the holes and improve the
13
14
134 steel-concrete interaction. The dimension of specimens are shown in Fig. 2(f) - (g).
15
16

135 2.2. Material properties

17
18
19
136 Tensile tests were done based on the guidelines specified in the Chinese code [23] to test the actual
20
21
22
137 properties of the steel tube. Table 2 listed the measured results of the tensile test.
23

24
138 Concrete cubes (150mm×150mm×150mm) and cuboids (150mm×150mm×300mm) were cast and
25
26
27
139 cured to test the axial strength, the elastic modulus and Poisson ratio. The compression test was
28
29
140 conducted according to the method in the Chinese standard [24]. The cubic strength of the concrete
30
31
141 f_{cu} was 65.6MPa. The corresponding elastic modulus and Poisson's ratio were 33,270MPa and 0.19,
32
33
142 respectively.
34
35

143 2.3. Test setup

144 2.3.1 Axially loaded specimens

145 The test machine with the capacity of 10,000 kN was used for the axial experiments in the
146 laboratory of Harbin Institute of Technology. For specimens CSW-T-1, CSW-T-2, CSW-T-4 and
147 CSW-T-5, the axial load was applied monotonously. For specimens CSW-T-3 and CSW-T-6, the axial
148 load was applied cyclically.
149

150 The tests were controlled by a load with a speed of 0.05 MPa/s before the yielding displacement.
151 The yielding displacement can be confirmed in the way specified as shown in Fig. 3 [25]. The load-
152 displacement curve was predicted by the finite element analysis before the experiments. When the
specimens yielded, the tests were switched to be controlled by the displacement with the rate of 10μm/s.
153
154
155
156
157
158
159

153 When the load decreased below 75% of the axial strength or the average strain (the measured
1
2
154 displacement divided by the height) reached 50000 $\mu\epsilon$, the tests were terminated.

4
155 For specimens CSW-T-3 and CSW-T-6 subject to cyclical axial load, the first unloading point is
6
7
156 the yielding displacement. Beyond the yielding displacement, the increment of the displacement is in
8
9
1057 pace with the yielding displacement. Thus, the loading speed and the unloading speed are the same
11
12
158 during each step.
13

159 2.3.2 Seismic specimens

16
1760 The 1,000 kN multi-functional actuator and 3,600 kN jack were used to apply the lateral load and
18
19
2061 the vertical load respectively. Fig. 4(a) and (b) showed the test setup. The shear walls were simplified
21
22
2062 as a cantilever member. A hinge was placed on the top of the specimens to ensure the specimens rotate
23
24
2063 freely. The axial load was applied by the jack and kept constant, as shown in Fig. 4(a). Rollers were
25
26
2064 set at the sides to prevent the possible out-plane deformation during the experiments. Besides, rollers
28
29
2065 on top of the specimens made the specimens move smoothly along the horizontal direction. The top
30
31
3066 beam was set to transfer the axial load and lateral load, as shown in Fig. 4 (c). The lateral actuator
33
34
3067 was connected to the specimens by the connected beam and top beam. The connected beam, top beam
35
36
3068 and load transducer are connected by high strength bolts, as shown in Fig. 4 (c). The strength of bolts
38
39
3069 could satisfy the tension requirement. The specimen was connected to the strong floor by the tie bars.
40
41
3070 The pretension load was added to the tie bars, which would guarantee that the specimen boundary
42
43
4071 could be fixed end. According to the analysis, two bars would be enough to connect the specimens to
45
46
3072 the floor, as shown in Fig. 4 (c).

48
4073 The axial load was applied in several steps and kept constant for 2 minutes in each step to observe
50
51
3074 the phenomena. The axial load applied to the specimens can be confirmed by $n_t=N/N_{exp}$, in which N_{exp}
52
53
5075 is the experimental result from axial experiments. The axial load N should be kept in a constant value
55
56
3076 until the experiment was finished.
57

58
5077 The lateral load was applied in the way specified in the Chinese specification [26]. Fig. 5 showed
60
61
62
63
64
65

178 the loading procedure. As shown, the lateral displacement was applied in four levels, 1/4, 2/4, 3/4,
1
2
179 and 1 of the yielding displacement before the specimens yielded. The yielding displacement was
3
4
180 determined in the same way as the axial experiments. Beyond the yielding displacement, the
5
6
181 increment of the displacement is the yielding displacement. The load would be applied for two cycles
7
8
9
182 at each level. The tests were terminated when the lateral force dropped to 85% of the ultimate load,
10
11
12
183 or the shear walls developed severe damage.
13

14 2.4. Instrumentation

15 2.4.1 Axially loaded specimens

16
17
185 The load was automatically recorded by the 10,000 kN compression machine. For the axial
18
19
20 experiments, four LVDTs were set at four corners to record the whole displacement during the tests.
21
22
23

24
188 To analyze the strain development of the steel plates, 24 strain gauges were stuck at the mid-height
25
26
189 of the specimens, as shown in Fig. 6(a).
27
28

29 2.4.2 Seismic specimens

30
31
191 The lateral load can be automatically recorded by the actuator as specified in Fig. 4(a). Eight
32
33
192 LVDTs were installed to measure the displacement of the feature points as shown in Fig. 7. The
34
35
193 displacement transducers LVDT-1~LVDT-3 were used to measure the lateral deformation along the
36
37
38 horizontal direction. The displacement transducers LVDT-4 and LVDT-5 were installed to measure
39
40
195 the possible rigid rotation of the whole specimens. LVDT-6 and LVDT-7 were used to quantify the
41
42
43 shear deformation subjected to the lateral loads. LVDT-8 was applied to measure the possible out-
44
45
196 plane displacements.
46
47

48
198 According to the buckling analysis in the finite element analysis, the local buckling would occur
49
50
199 at the height of 50 mm and 150 mm from the concrete surface in each partition. The strain gauges
51
52
200 were used to represent the development of steel stress of the steel tube. To analyze the strain
53
54
55 distribution and the stress development, strain gauges and strain rosettes were glued on the steel tube
56
57
201 at the height of 50 mm and 150 mm from the top surface of the RC rigid beam. The location of strain
58
59
202

203 gauges and strain rosettes was shown in Fig. 6(b). The strain gauges numbered in the brackets were
1
2
204 set at the height of 150 mm. The strain rosettes were stuck on the web as the shear stress might
3
4
205 influence the principal stress orientation. On surface 4 and surface 3, small values of strain gauges
6
7
206 were observed as the steel plate was mainly subjected to vertical stress.
8
9

1207 **3. Failure progression and modes**

1208 *3.1 Axially loaded specimens*

1209 To describe the phenomena clearly, the surfaces were numbered as shown in Fig. 8. All the axially
16
1210 loaded specimens experienced similar progress and appeared a similar failure mode. Taking specimen
18
19
211 CSW-T-1 as an example, the phenomena during the test were described in detail. The load-
20
21
2212 displacement curve was linear when the vertical strain of the steel plate was below 1500 $\mu\epsilon$, which
23
24
213 can be seen as the elastic stage of the specimen. A slight sound can be heard when the load was about
25
26
2214 500 kN, which may be due to the loss of the steel-concrete adhesion. As the load increased to 5900
28
29
215 kN, the steel plate at the mid of the surface 1 and surface 2 buckled firstly as illustrated in Fig. 9(a).
30
31
3216 When the specimen reached the axial compression, the local buckling was observed on surface 4 as
33
34
217 specified in Fig. 9(b). As the displacement applied on the specimens increased, the local buckling
35
36
3218 mentioned above further deteriorated, resulting in more severe deformation as shown in Fig. 9(c) -
38
39
219 (d). Besides, the inner concrete was damaged where the local buckling appeared as shown in Fig. 9(e)
40
41
220 - (f).
42
43

421 For the specimens with different heights, the load-carrying capacity decreased as the local buckling
45
46
222 occurred. However, the higher specimens failed with less local buckling as shown in Fig. 9(g). In
47
48
4223 addition, the weld of the flange cracked, which may be resulted from the second-order effect as shown
50
51
224 in Fig. 9(h).
52
53

525 For different load applied modes, phenomena of specimens with the height of 300 mm were similar
55
56
226 to each other. While, for the specimens with the height of 500 mm, the welding fracture started earlier
57
58
527 when the load was applied cyclically. This may be due to the damage accumulation and second-order
60
61
62
63
64
65

228 effect, which made the stress concentration severe and caused the weld cracking.

229 3.2 Seismic specimens

230 The axial loads applied on specimens CSW-T-03 and CSW-T-05 were 2000 kN and 3000 kN,
231 respectively. According to the tests of short specimens, the behavior of specimens with a height of
232 500 mm would be affected by the second-order effect. Thus, the axial strength of such section should
233 be seen as 6448 kN. The specimens all experienced the progression of local buckling, concrete
234 crushing and welding fracture.

235 For the specimen CSW-T-03, the load increases linearly with the increase of lateral displacement
236 before the cycle of 12 mm (the drift angle of 1/67). The drift angle is calculated by dividing the lateral
237 displacement by the height of the specimens. At the cycle of 1/67, the local buckling firstly occurred
238 at the bottom of surface 4 and 6 as shown in Fig. 10(a). When it came to the displacement of 15 mm
239 (the drift angle of 1/53), the lateral load reached its peak strength in the positive direction, the steel
240 plate at the bottom of surface 1 and surface 2 began to buckle.

241 As the drift angle increased, the steel plate buckled along the bottom of the surfaces at two heights
242 of about 50 mm and 150 mm as shown in Fig. 10(a). At the cycle of 1/44 (displacement of 18 mm)
243 in the positive direction, the weld between the surface 4 and 6 was cracked and the load-carrying
244 capacity decreased suddenly. Thus, the load procession in the positive direction was terminated.
245 Along the negative load direction, the lateral load was applied cyclically until the lateral load dropped
246 below 85% of the peak load. The failure mode of specimen CSW-T-03 was shown in Fig. 11(a).

247 Compared with specimen CSW-T-03, specimen CSW-T-05 has experienced a simpler failure mode.
248 While the local buckling appeared earlier for CSW-T-05 at the cycle of 1/160 with the displacement
249 of 5 mm as shown in Fig. 10(b). The weld was also cracked on the flange as shown in Fig. 11(b). The
250 failure mode was shown in Fig. 11(b). As shown in Fig. 11(b), the deformation of the steel plate
251 concentrated on the flange.

252 The inner concrete was crushed and the crushing zone was concentrated at the flange as shown in

253 Fig. 12. The capacity of specimens did not drop too much while the crushing of concrete was severe,
1
2
254 as the steel tube could confine the concrete well.
3
4

255 4. Test results and discussions 6

256 4.1 Characteristic curves of axially loaded specimens 7 8

257 The load to vertical strain curve can represent some character indices of the specimens. The axially
11
12
258 experimental curves were presented in Fig. 13. As shown, the curves in each group were similar in
13
14
259 stiffness and axial strength. It can be found that different modes of load almost had no influence
16
17
260 before the peak load was attained, as the multi-partition steel tube could confine the concrete well.
18
19
261 For the specimens CSW-T-3 and CSW-T-6, the cyclic load may lead to the termination of the
20
21
262 experiment at earlier displacement (about 15000 $\mu\epsilon$) as the second-order effect and the concrete
23
24
263 damage would be severe. Table 3 showed the key indices of the specimens. The axial strength of
25
26
264 specimens with the height of 500 mm was about 92% of specimens with the height of 300mm.
28

265 The load capacity of such a section, which was the sum of the concrete and the steel strength
30
31
3266 (calculated by $N_s=f_cA_c+f_yA_s$), was about 5029 kN. f_c could be calculated from f_{cu} in the way specified
33
34
267 in Mirza [27]. Compared with N_s , the axial strength P_{max} in Table 3 had enhanced about 28% and 18%
35
36
268 for CSW-T-1-CSW-T-3 and CSW-T-4-CSW-T-6 respectively. For the specimens CSW-T-3 and CSW-
38
39
269 T-6, the unloading stiffness and the reloading stiffness were almost the same as shown in Fig. 13.
40
41
270 Besides, the unloading curves and reloading curves would not be overlapped well as the plastic
42
43
44
45
46
471 deformation developed.

472 The trend of strain gauges was similar for the axially loaded specimens. In this paper, the stress
48
49
273 analysis of specimen CSW-T-1 was used as an example to describe the results of the strain gauges
50
51
274 reading during the experiment. The stress of the steel plates calculated in the way of Zhang [28] was
52
53
275 shown in Fig. 14, including the vertical stress σ_v , the horizontal stress σ_h and the equivalent stress σ_z .
55
56
276 The stresses on the steel plate and pipe were calculated based on the measured data of strain gauges
57
58
277 numbered 3 and 4, 1 and 2, respectively. For the steel pipe, the steel-concrete adhesion may cause
60
61
62
63
64
65

278 that the horizontal stress of the steel pipe was in a compressive condition when the load applied on
1
279 the specimens was not very high as shown in Fig. 14(b). In addition, the horizontal stress of the steel
2
3
4
280 plate was in a high value because of the interaction between the different parts as shown in Fig. 14(a).
5
6
281 The multi-partition steel tube including the steel plate and the steel pipe yielded at the load of around
7
8
9
1282 5000 kN as shown in Fig. 14. When the specimens reached the axial strength, the horizontal stress of
10
11
1283 steel pipe was larger than that of steel plate, which meant the concrete confinement of steel pipe was
12
13
14
1284 better as the width-to-thickness ratio of steel pipe was less.
15
16

1285 The ductility of the specimen was determined by Eq. 1. The results are specified in Table 3. For
17
18
19
1286 specimens CSW-T-1-CSW-T-3, the ductility was similar when the load mode was the same. While
20
21
2287 the ductility would reduce when the load was applied cyclically. For specimens CSW-T-4 to CSW-T-
22
23
24
2288 6, the ductility was similar although the load mode was different. That means the load mode may
24
25
26
2289 have little impact on the key index of specimens. However, the ductility would be lower when the
27
28
29
290 height increased. This may be caused by the influence of the second-order effect.
30
31

$$3291 \mu = \Delta_u / \Delta_y \quad (1)$$

3292 4.2 Hysteretic curves and skeleton curves of seismic specimens

3293 The hysteretic curve, the relationship between the lateral displacement and the lateral load, can
34
35
36
3294 show the basic performance of the component subjected to the lateral load. Fig.15 showed the
37
38
39
3295 hysteretic curves of specimens CSW-T-03 and CSW-T-05. As shown, the hysteretic curves were both
40
41
42
43
4296 full and stable, which meant that this kind of shear wall exhibited a good ability for resisting the
44
45
46
4297 lateral load. The loop area of specimen CSW-T-05 was larger than that of specimen CSW-T-03 as
47
48
4298 shown in Fig. 16. As the axial load ratio increased, the ability to resist the cyclical lateral load would
49
50
51
5299 be better as the inner steel plate could confine the concrete effectively [18]. In addition, the hysteretic
52
53
54
5300 curve was asymmetric as the load capacity would be different in the positive and negative directions.
55

5301 The shear deformation could be peeled from the total deformation according to the data measured
56
57
58
5302 by LVDT-6 and LVDT-7 [29]. Eq. 2 shows how to calculate the shear deformation.
59
60
61
62
63
64
65

$$\gamma = \frac{(u_7 - u_6)\sqrt{a^2 + b^2}}{2ab} \quad (2)$$

where u_6 and u_7 are displacements measured by LVDT-6 and LVDT-7, respectively; a and b are the width and height of the area covered by LVDT-6 and LVDT-7, respectively.

As shown in Fig. 17, it can be found that the shear deformation was about 40% of the total deformation. When the lateral displacement increased, the shear deformation became abnormal, which may be caused by the local buckling of the steel tube. According to the experimental phenomenon and shear deformation data, tension bands were developed in the middle web when the specimen was destroyed. The rolled square pipe and flanges were in a compression state, and local buckling failure occurred in the steel tubes. Therefore, the failure mode was a flexural-shear failure.

The backbone curve is the relationship between the peak load and the corresponding displacement at each cycle of the hysteretic curves. Fig.18 was the comparison of two lateral cyclically loaded specimens. As shown, the initial stiffness of the specimen CSW-T-05 was higher than that of specimen CSW-T-03. Moreover, the lateral capacity was higher with increasing of the axial load ratio. However, the shear strength of specimen CSW-T-05 decreased faster than that of CSW-T-03 in the descending branch as shown in Fig. 18, which indicated that the ductility of the specimen decreased when the axial load ratio increased.

4.3 Deformation analysis of seismic specimens

The key indices of the seismic specimens, which could be confirmed from the backbone curves as shown in Fig. 18, were specified in Table 4. As it showed, the ductility would decrease as the axial load increased. Compared with the value specified in the Chinese code [22], the design axial load ratio n_d of specimens CSW-T-03 and CSW-T-05 in this paper was much larger than the limitation of 0.5. However, the elastic drift angle (1/151 and 1/160) and the elastic-plastic ratio (1/66 and 1/61) were larger than the limitation of 1/400 and 1/80, respectively, as shown in Fig. 18. That meant such kind of shear walls possessed good ability in resisting the lateral load and satisfied the requirement of the Chinese code well.

328 4.4 Stiffness degradation of seismic specimens

1
2
329 The cyclic stiffness K_j of the cyclic specimens could be calculated by Eq.3 [30]. The cyclic stiffness
4
330 means the average secant rigidity of the specimen during the cycles. Fig. 19 presents the curves
6
331 combined by the cyclic stiffness and the laterally top displacement. The stiffness of specimen CSW-
8
9
332 T-05 was higher than that of specimen CSW-T-03. This could be explained that the axial load would
11
12
333 restrain the development of the tensile area, which would benefit the stiffness. In the early stage
13
14
334 (before the yielding displacement of 5 mm), the trends of stiffness degradation were similar. As the
16
17
335 displacement developed, the stiffness decreased faster when the axial load ratio increased. That meant
18
19
336 the ductility decreased when the axial load ratio increased. This result has coincided with the analysis
21
22
337 of the deformation.

$$23$$
$$24$$
$$25$$
$$26 K_j = \frac{\sum_{i=1}^{n_j} P_j^i}{\sum_{i=1}^{n_j} \Delta_j^i} \quad (3)$$
$$27$$

28
29 where P_j^i and Δ_j^i are the peak load and the corresponding displacement at the i th cycle of the j th
30
31
338 drift angle, respectively; n_j means the number of cycles at the j th drift angle level.

339 4.5 Strength degradation of seismic specimens

34
35
336 Unlike the static experiment, it was the progress of damage accumulation for the seismic
37
38
337 experiments. Moreover, the accumulative damage would influence the hysteretic curves even the
39
40
338 curves were in the same drift angle level. That may cause the peak strength at the second cycle of the
41
42
339 same drift angle to decrease. The strength reduction factor η_j can be calculated by Eq. 4 [31].

$$43$$
$$44$$
$$45$$
$$46 \eta_j = \frac{P_j^2}{P_j^1} \quad (4)$$
$$47$$
$$48$$

49
50 where P_j^i is the maximum load at i th cycle of j th displacement level.

51
52
340 Fig. 20 were the curves of the strength reduction factor and the drift angle of specimens CSW-T-
53
54
341 03 and CSW-T-05. As shown, the strength reduction factor was around 0.9-1.0. That meant the multi-
55
56
342 partition steel tube could restrain the concrete in good condition, even under a high-stress state. The
57
58
343 strength reduction factor did not decrease continuously when the lateral displacement applied to the

352 specimens increased. This could be seen as the progress of concrete crushing and stress redistribution.

353 4.6 Energy absorption capacity of seismic specimens

354 The energy dissipation coefficient E determined by Eq. 5 [32] could represent the energy
355 dissipation capacity. Fig. 21 shows the way for calculating the energy dissipation coefficient.

$$356 E = \frac{S_{ABC} + S_{CDA}}{S_{OBE} + S_{ODF}} \quad (5)$$

357 where S_{ABC} and S_{CDA} are the areas circled by the hysteretic curve and the displacement axis; S_{OBE}
358 and S_{ODF} are the triangular areas as illustrated in Fig. 21.

359 Fig. 22 showed curves of the energy dissipation coefficient and the lateral drift angle. Before the
360 yielding load (about the drift angle of 0.5%), the energy dissipation coefficients of the two specimens
361 were close, which were not very high as the plastic damage did not appear obvious. As the lateral
362 displacement developed, the energy dissipation coefficient became larger. As shown, E was larger as
363 the axial load ratio was higher, which meant the plastic deformation was more severe for specimen
364 CSW-T-05. That meant the multi-partition steel tube could not only resist the concrete from crushing
365 but also work as the mechanism of steel tube confined concrete columns [33].

366 4.7 Stress analysis of seismic specimens

367 For specimen CSW-T-03, Fig. 23 showed the stress calculated in the way specified in Zhou [34]
368 under different drift angles. As shown, the relationship between the Von-Mises stress and the drift
369 angle was not linear. Besides, it could be found that the steel tube of the web yielded earlier than that
370 of the flange as the area of the flange was larger for resisting the lateral load combined with the axial
371 load. The multi-partition steel tube yielded along the whole section when the experiment terminated.

372 5. Comparison between experimental and calculated results

373 5.1 Comparison of axially loaded specimens

374 As the T-shaped shear wall was composited by some square columns, the design details specified
375 in some codes can be used to calculate this new type shear walls conservatively. For the axial strength
376 of the specimens, Eq. 6, Eq. 7, and Eq. 8 are the design formula specified in the European code [35],

377 Chinese code (CECS) [36], and American code (AISC) [37], respectively.

$$378 \quad N = A_c f_{ck} + A_s f_s \quad (6)$$

379 where f_{ck} is the compressive concrete strength calculated by $0.76f_{cu}$.

$$380 \quad N = A_c f_c + A_s f_s \quad (7)$$

$$381 \quad N = 0.85 A_c f_c + A_s f_s \quad (8)$$

382 The calculated results were listed in Table 5. According to the specifications in design codes
383 mentioned above, for the axially loaded stub specimens, the second order-effect was ignored. As the
384 height-to-breadth ratio of tested specimens was only 3 and 5, all of them could be seen as stub
385 specimens. Thus, the design axial strengths of the specimens with different heights were all the same.
386 As shown, the strength capacities calculated by the codes were lower than the experimental results,
387 which meant the design method was conservative.

388 5.2 Comparison of seismic specimens

389 For the seismic experiment, the specimens would suffer bending moment caused by the lateral load
390 combined with axial load. According to the specification for the combined flexure and axial force,
391 the $M-N$ relationship curves of different codes of the section were shown in Fig. 24. It shows that the
392 capacities in the two directions are different. The capacities from experiments are also shown in Fig.
393 24. It can be found that the design methods specified in the codes were conservative, as the
394 experimental results were higher than the calculated results based on design codes. Among them, the
395 method of EC4 can estimate the capacity of flexure combined with axial load better.

396 6. Conclusions

397 The experimental study of T-shaped composite shear walls was the main work of this research. The
398 multi-partition steel tube was used to form the T-shaped shear walls. Six axially static experiments
399 and two seismic experiments were conducted to investigate damage progression, strength, ductility,
400 and failure mode of this new type of wall. In addition, the results of the experiments were compared
401 with those of design codes. According to the experimental results, the conclusions were as follows.

- Axially loaded specimens exhibited high strength and good ductility. When the height changes from 300 mm to 500 mm, the axial strength is almost the same. However, the ductility decreased. Axially static and cyclic loading modes had little influence on the stiffness and axial strength.
- The novel T-shaped composite shear walls performed asymmetrical behavior along with positive and negative directions. Such shear walls possessed good lateral resistance and energy dissipation capacity, and even the design axial load ratio was 0.93. As the axial load ratio increased, the energy dissipation capacity and the lateral resistance increased while the ductility decreased obviously.
- Because of the confinement of the steel tube to the core concrete, the bearing capacity of the specimen was higher than the sum of steel strength and concrete strength. The results of the experiments were compared to those calculated by some design codes. The results of the design codes were smaller than the experimental results. Among the codes AISC, EC4, and CECS, the capacities of the specimens under combined flexural and axial load are well assessed by the EC4 code.

Acknowledgments

The authors sincerely thank the support from the National Natural Science Foundation of China (Grant No. 51578187) and the National key research and development program (2016YFC0701201).

The people who participated in this research and the help from the key lab should be remembered.

References

- [1] Lai Z.C., Varma Amit H., Zhang K. Noncompact and slender rectangular CFT members: Experimental database, analysis, and design. *J Constr Steel Res* 2014; 101: 455-468.
- [2] Wang Z.B., Tao Z., Han L.H., et al. Strength, stiffness and ductility of concrete-filled steel columns under axial compression. *Eng Struct* 2017; 135: 209-221.
- [3] Wang J.T., Wang F.C. Analytical behavior of built-up square concrete-filled steel tubular columns

- 427 under combined preload and axial compression. *Steel Compos Struct* 2021; 38(6): 617-635.
- 428 [4] Rahaman A., Anik A.M., Kamrujjaman Serker N.H.M. Effect of special shaped column on lateral
429 load resistance capacity of reinforced concrete (RC) building. *American Journal of Civil
430 Engineering*, 2018, 6(5):147-153.
- 431 [5] Gumble A.N., Pajgade P.S. Comparison between specially shaped columns and rectangular
432 columns in RC structures. *International Journal of Advance Engineering and Research
433 Development*. 2015; 2(5): 679-684.
- 434 [6] Hsu C.T.T. T-Shaped Reinforced Concrete Members under biaxial bending and axial
435 compression. *ACI Struct J* 1989; 86: 460-468.
- 436 [7] Li B., Pham T.P. Experimental Study on the Seismic Response of L-Shaped Reinforced Concrete
437 Columns. *Structures Congress* 2013.
- 438 [8] Zhou T., Chen Z.H., Liu H.B.. Seismic behavior of special shaped column composed of concrete
439 filled steel tubes. *J Constr Steel Res* 2012; 75: 131-141.
- 440 [9] Yang Y.B., Yang H., Zhang S.M. Compressive Behavior of T-shaped Concrete Filled Steel
441 Tubular Columns. *Int J Steel Struct* 2010; 10: 419-430.
- 442 [10] Tu Y.Q., Shen Y.F., Zeng Y.G., et al. Hysteretic behavior of multi-cell T- Shaped concrete-filled
443 steel tubular columns. *Thin-Walled Struct* 2014; 85: 106-116.
- 444 [11] Tu Y.Q., Shen Y.F., Li P. Behaviour of multi-cell composite T-shaped concrete-filled steel tubular
445 columns under axial compression. *Thin-Walled Struct* 2014; 85: 57-70.
- 446 [12] Yang Y.L., Wang Y.Y., Fu F. Static behavior of T-shaped concrete-filled steel tubular columns
447 subjected to concentric and eccentric compressive loads. *Thin-Walled Struct* 2015; 95: 374-388.
- 448 [13] Liu X.G., Xu C.X., Liu J.P., et al. Research on special-shaped concrete-filled steel tubular
449 columns under axial compression. *J Constr Steel Res* 2018; 147: 203-223.
- 450 [14] Zuo Z.L., Cai J., Chen Q.J., et al. Performance of T-shaped CFST stub columns with binding bars
451 under axial compression. *Thin-Walled Struct* 2018; 129: 183-196.
- 452 [15] Zhang X.M., Qin Y., Chen Z.H., Experimental seismic behavior of innovative composite shear

- 453 walls. J Constr Steel Res 2016; 116: 218-232.
1
- 454 [16]Zhang X.M., Qin Y., Chen Z.H., et al. Experimental behavior of innovative T-shaped composite
2
3
4
455 shear walls under in-plane cyclic loading. J Constr Steel Res 2016; 120: 143-159.
5
6
- 456 [17]Qin Y., Shu G.P., Zhou X.L., et al. Behavior of T-shaped sandwich composite walls with truss
7
8
9
457 connectors under eccentric compression. J Constr Steel Res 2020; 169: 106067.
10
- 458 [18]Guo L.H., Wang Y.H., Zhang S.M.. Experimental study of rectangular multi-partition steel-
11
12
13
459 concrete composite shear walls. Thin-Walled Struct 2018; 130: 577-592.
14
15
- 460 [19]Shi J., Guo L.H., Gao S., et al. Buckling behavior of double skin composite walls under axial
16
17
18
461 compressive load[J]. Construction and Building Materials 2022, 321: 126345.
19
- 462 [20]Shi J., Guo L.H., Qu B. In-plane cyclic tests of double-skin composite walls with concrete-filled
20
21
22
463 steel tube boundary elements. Engineering Structures 2022; 250: 113301.
23
24
- 464 [21]Nie J.G., Hu H.S., Fan J.S., et al. Experimental study on seismic behavior of high-strength
25
26
27
465 concrete filled double-steel-plate composite walls. J Constr Steel Res 2013; 88: 206-219.
28
29
- 466 [22]Ministry of Housing and Urban-Rural Development of the People’s Republic of China
30
31
32
467 (MOHURD), JGJ/T 380-2015: Technical specification for steel plate shear walls, Beijing (2015).
33
- 468 [23]General Administration of Quality Supervision, Inspection and Quarantine of the People's
34
35
36
469 Republic of China (AQSIQ), GB/T 228.1-2010: Metallic materials-Tensile testing-Part 1:
37
38
470 Method of test at room temperature, (2010).
39
40
- 471 [24]Ministry of Housing and Urban-Rural Development of the People’s Republic of China
41
42
43
472 (MOHURD), GB/T 50081-2002: Standard for test method of mechanical properties on ordinary
44
45
473 concrete, Beijing (2003).
46
47
- 474 [25]Tao M.X., Fan J.S., Nie J.G. Seismic behavior of steel reinforced concrete column-steel truss
48
49
50
51
475 beam hybrid joints. Eng Struct 2013; 56: 1557-1569.
52
- 476 [26]Ministry of Housing and Urban-Rural Development of the People’s Republic of China
53
54
55
477 (MOHURD), JGJ/T 101-2015: Specification for seismic test of building, Beijing (2015).
56
57
- 478 [27]Mirza S.A., Lacroix E.A. (2004), “Comparative strength analyses of concrete-encased steel
58
59
60
61
62
63
64
65

479 composite columns”, J Struct Eng, 130 (12): 1941-1953.
1
2
3
4
480 [28]Zhang S.M., Guo L.H., Ye Z.L., et al. Behavior of steel tube and confined high strength concrete
5
6
481 for concrete-filled RHS tubes. Adv Struct Eng 2005; 8: 101-116.
7
8
482 [29]Beyer K., Dazio A., Nigel Priestley M.J. Shear Deformations of Slender Reinforced Concrete
9
10
483 Walls under Seismic Loading. ACI Struct J 2011; 108: 167-177.
11
12
484 [30]Ji X.D., Jiang F.M., Qian J.R. Seismic behavior of steel tube-double steel plate-concrete
13
14
485 composite walls: Experimental tests. J Constr Steel Res 2013; 86: 17-30.
15
16
486 [31]Yan J.B., Li Z.X., Wang T. Seismic behaviour of double skin composite shear walls with
17
18
487 overlapped headed studs. Constr Build Mater 2018; 191: 590-607.
19
20
488 [32]Guo L.H., Qong Q., Qu B., et al. Testing of steel plate shear walls with composite columns and
21
22
489 infill plates connected to beams only. Eng Struct 2017; 136: 165-179.
23
24
490 [33]Zhang S.M., Liu J.P. Seismic behavior and strength of square tube confined reinforced-concrete
25
26
491 (STRC) columns. J Constr Steel Res 2007; 63: 1194-1207.
27
28
492 [34]Zhou X.H., Zhou Z., Gan D. Cyclic testing of square tubed-reinforced-concrete column to RC
29
30
493 beam joints. Eng Struct 2018; 176: 439-454.
31
32
494 [35]European Committee for Standardization (CEN), EN 1994-1-1: Eurocode 4: Design of composite
33
34
495 steel and concrete structures, part 1-1: general rules and rules for buildings, Brussels (2004).
35
36
496 [36]China Association for Engineering Construction Standardization (CECS), CECS 159: 2004:
37
38
497 Technical specification for structures with concrete-filled rectangular steel tube members,
39
40
498 Beijing (2004).
41
42
499 [37]American Institute of Steel Construction (AISC), AISC 360-16: Specification for structural steel
43
44
500 buildings, Chicago (IL) (2016).
45
46
47
48
49
50
51
52
53
54
55
56
57
58
59
60
61
62
63
64
65

Figures

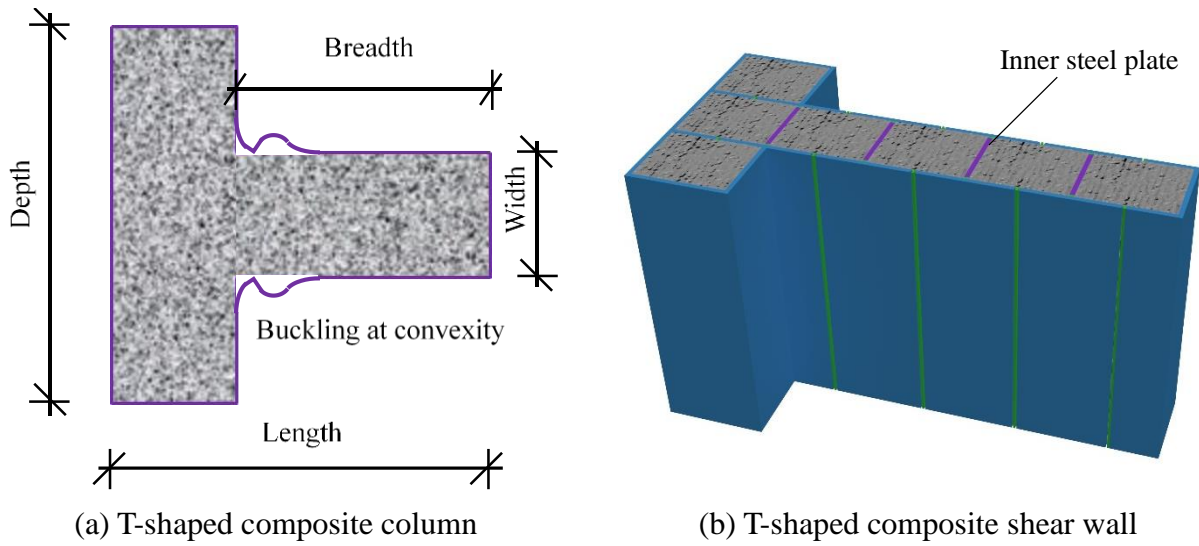
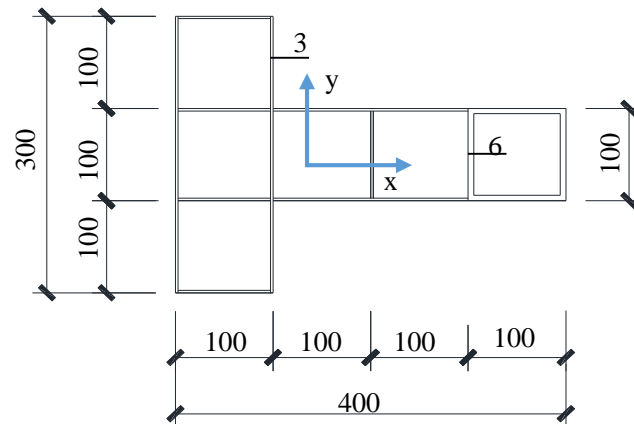
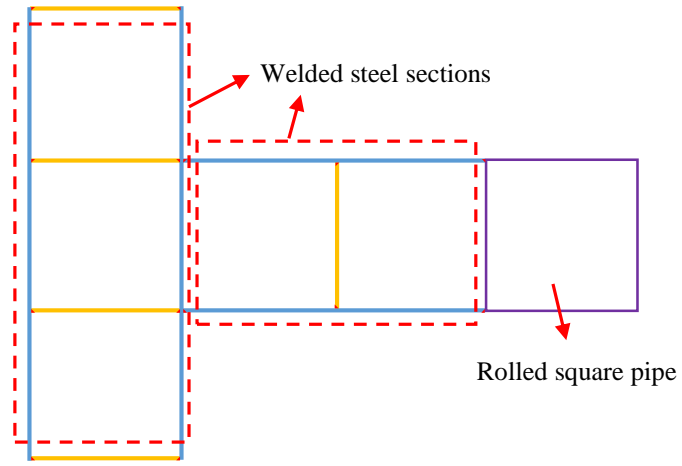


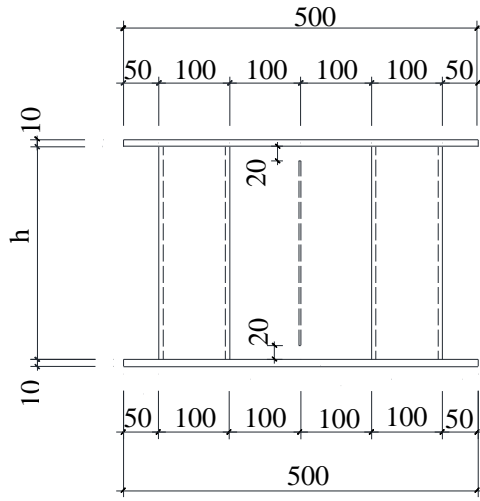
Fig. 1 Cross-section of special-shaped component



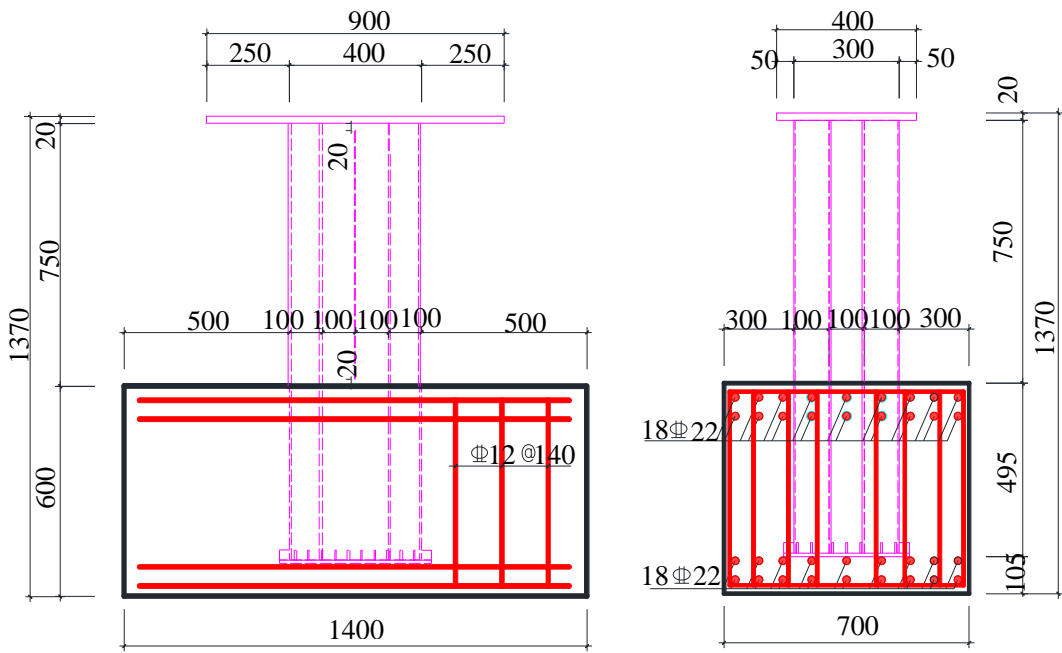
(a) Cross section



(b) Ways for fabrication

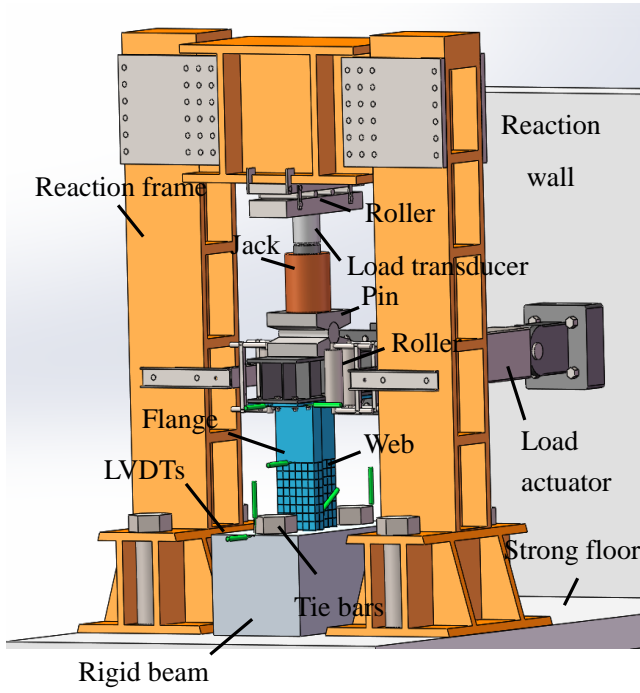


(c) Front view of CSW-T-1



(d) Front view of CSW-T-03 and CSW-T-05

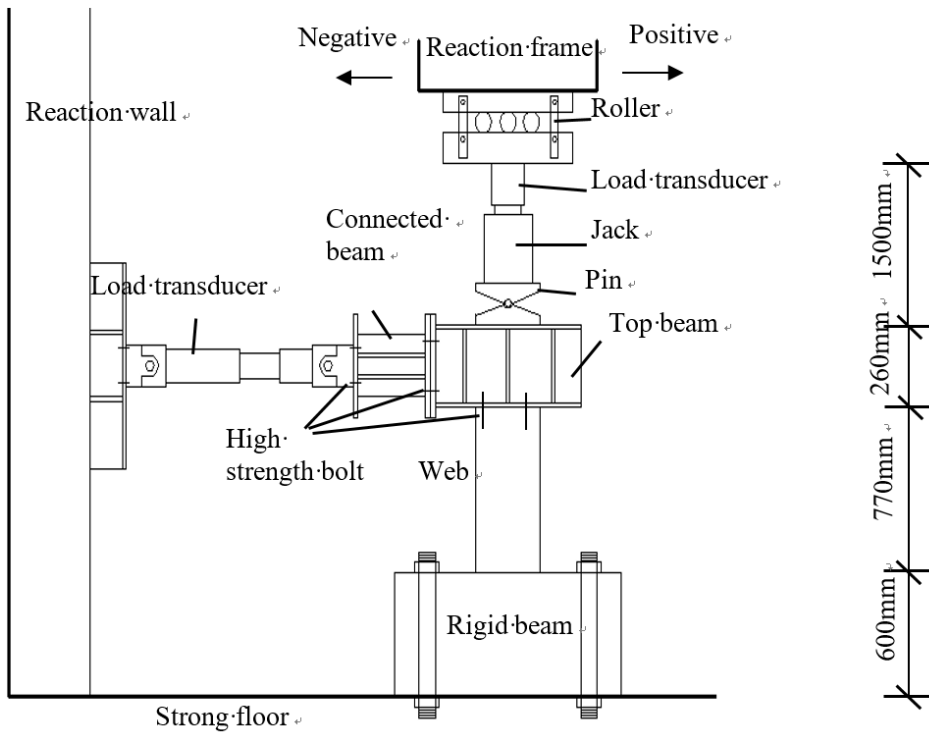
(e) Side view of CSW-T-03 and CSW-T-05



(a) Detailed information



(b) Overall information



(c) Perspective view

Fig. 4 Test set up for seismic experiments

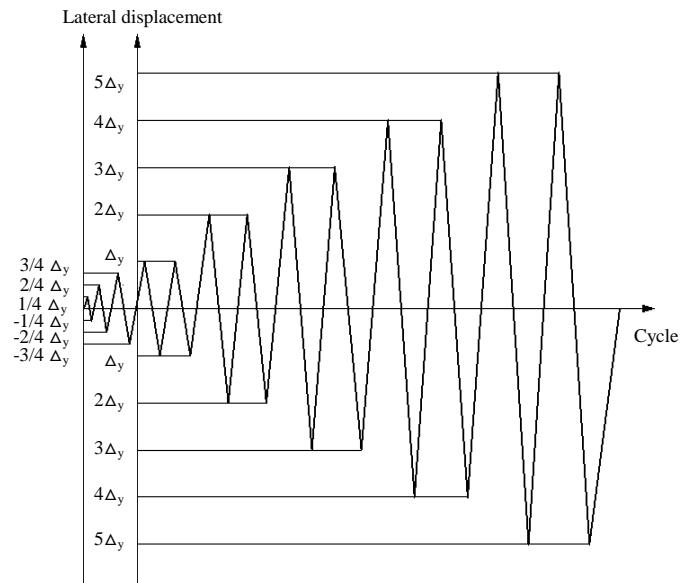
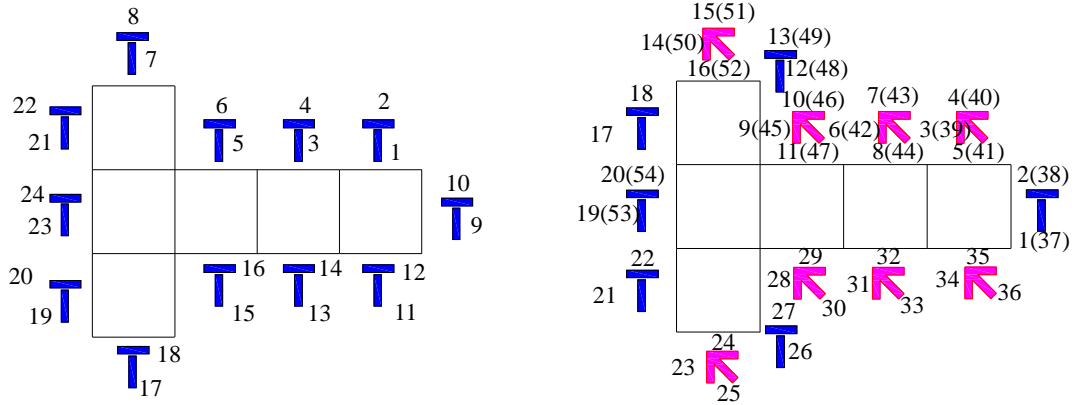


Fig. 5 Loading history of cyclic load



(a) Axial specimens

(b) Seismic specimens

Fig. 6 Distribution of strain gauges and strain rosettes

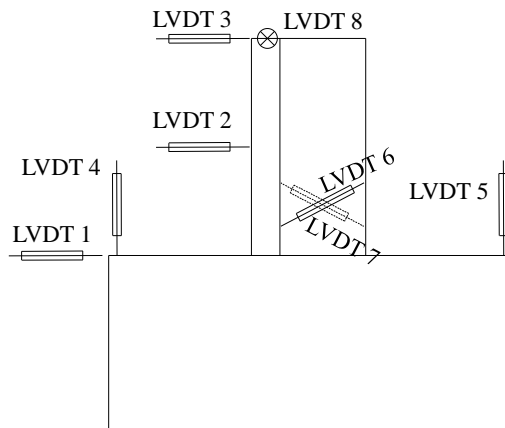


Fig. 7 Arrangement of LVDTs

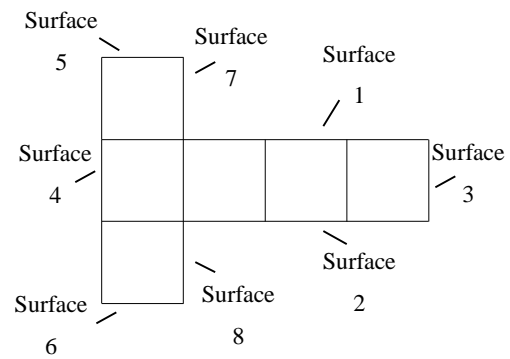
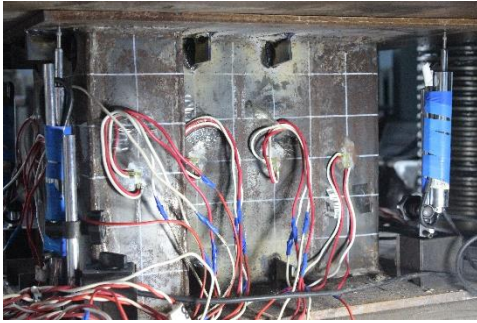


Fig. 8 Surface of specimens



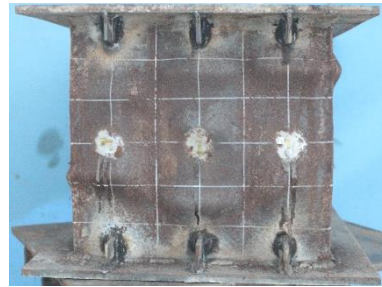
(a) Buckling mode of specimen CSW-T-1 in the test (web)



(b) Buckling mode of specimen CSW-T-1 in the test (flange)



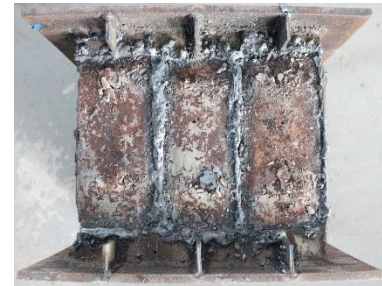
(c) Buckling mode of specimen CSW-T-1 (web)



(d) Buckling mode of specimen CSW-T-1 (flange)



(e) Concrete crush of specimen CSW-1 (front)



(f) Concrete crush of specimen CSW-1 (flange)



(g) Buckling mode of specimen CSW-T-4 (web)



(h) Buckling mode of specimen CSW-T-4 (flange)

Fig. 9 Failure mode of specimens CSW-1 and CSW-4

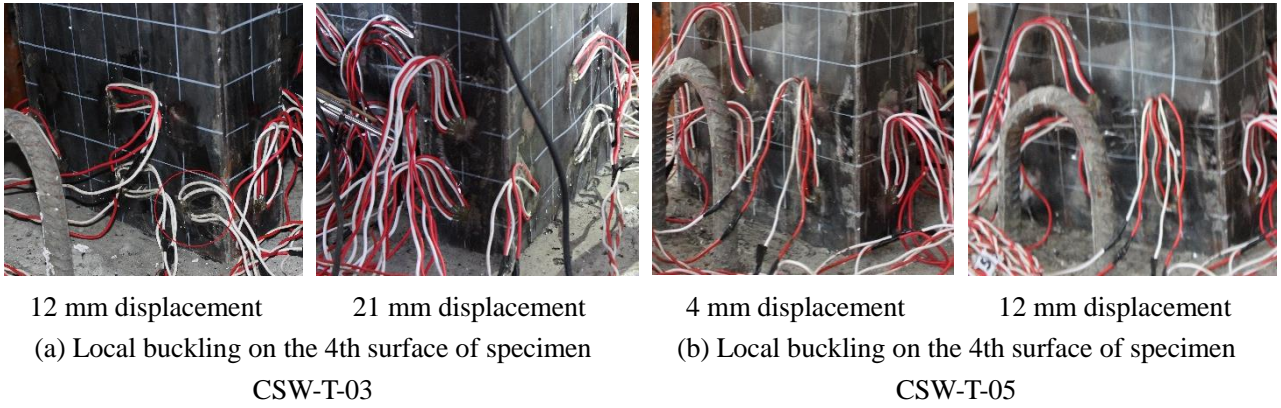


Fig. 10 Local buckling of steel plate



Fig. 11 Failure mode of specimens CSW-T-03 and CSW-T-05



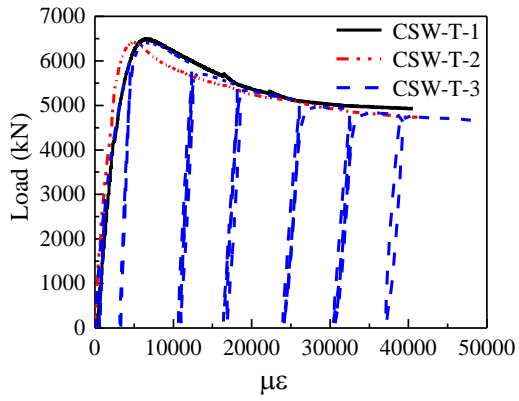


(c) Side view of CSW-T-03

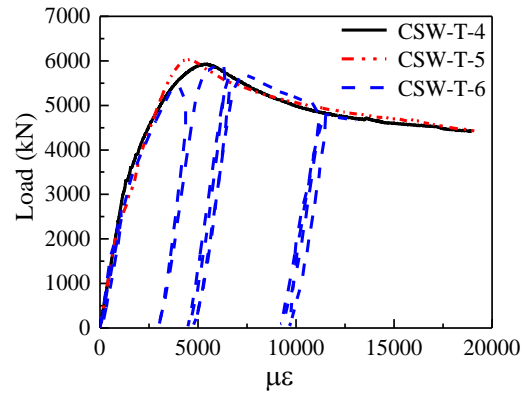


(d) Side view of CSW-T-05

Fig. 12 Phenomena of inside concrete after removing steel plate

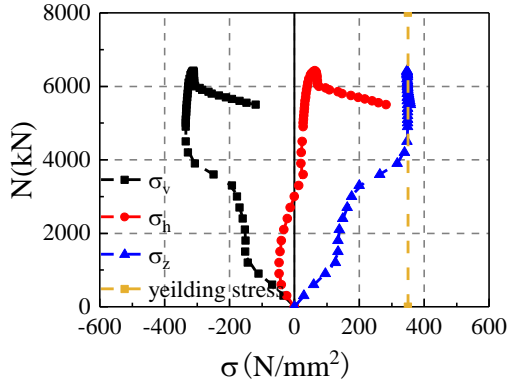


(a) Specimens with height of 300 mm

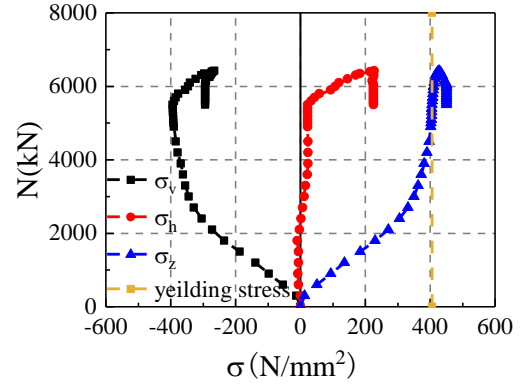


(b) Specimens with height of 500 mm

Fig. 13 Load versus axial strain relationship curves

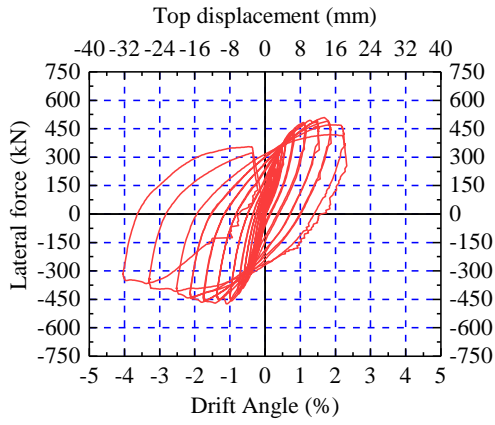


(a) Steel plate of CSW-T-1

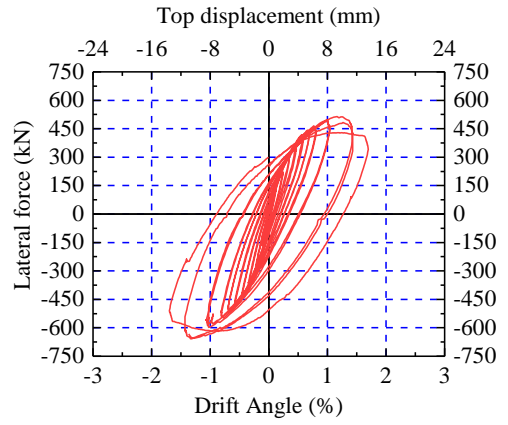


(b) Steel pipe of CSW-T-1

Fig. 14 Stress of multi-partition steel tube of specimen CSW-T-1



(1) CSW-T-03



(8) CSW-T-05

Fig. 15 Hysteretic curves

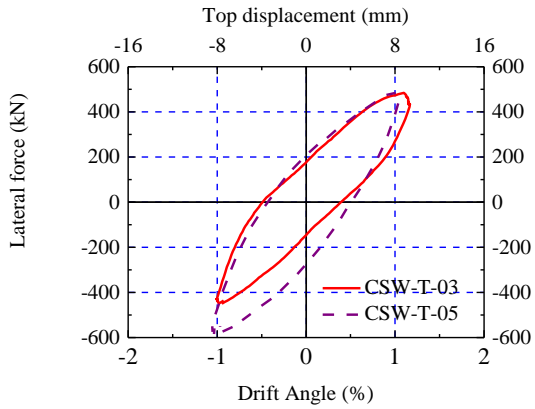


Fig. 16 Comparison of hysteretic curves

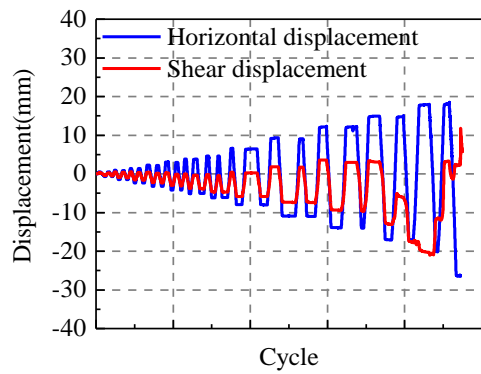


Fig. 17 Comparison of shear displacement and total horizontal displacement of specimen CSW-T-03

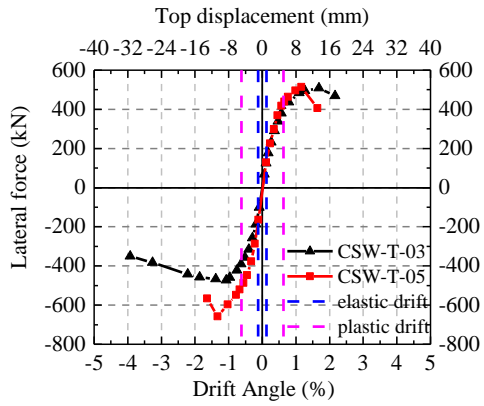


Fig. 18 Envelop curves of hysteretic loops

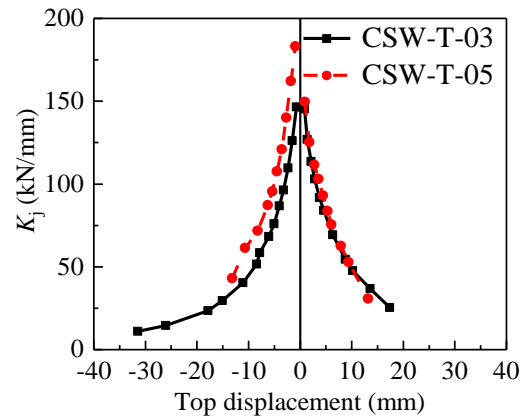


Fig. 19 Cyclic stiffness versus top displacement

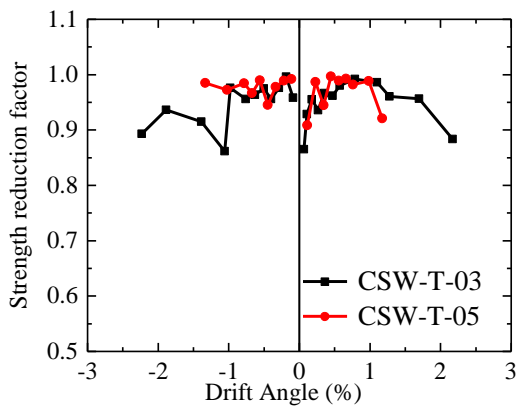


Fig. 20 Strength reduction of seismic specimens

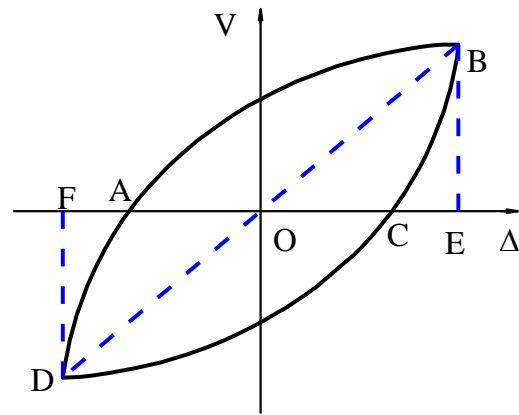


Fig. 21 Calculation diagram of energy absorption coefficient

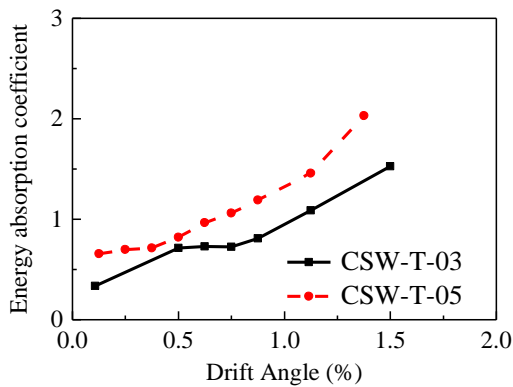


Fig. 22 Energy absorption coefficient for seismic specimens

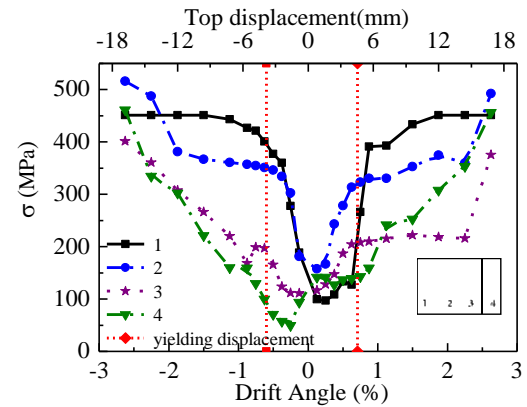
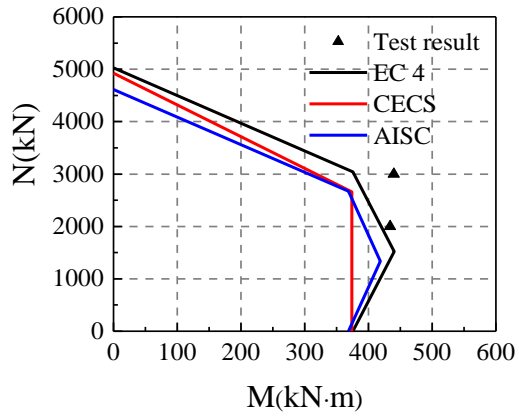
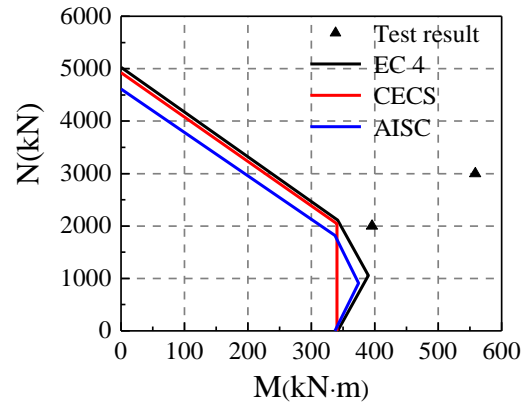


Fig. 23 Stress of CSW-T-03



(a) Positive direction



(b) Negative direction

Fig. 24 Comparison of design codes and test results

Tables

Table 1 Design parameters of all specimens

<i>no.</i>	Height (mm)	Depth of Flange (mm)	Breadth of Web (mm)	Width (mm)	Axial load ratio n_t	Design axial load ratio n_d	Axial load (kN)	Axial load mode
CSW-T-1	300	300	300	100	-	-	-	monotonic
CSW-T-2	300	300	300	100	-	-	-	monotonic
CSW-T-3	300	300	300	100	-	-	-	cyclic
CSW-T-4	500	300	300	100	-	-	-	monotonic
CSW-T-5	500	300	300	100	-	-	-	monotonic
CSW-T-6	500	300	300	100	-	-	-	cyclic
CSW-T-03	750	300	300	100	0.31	0.62	2000	constant
CSW-T-05	750	300	300	100	0.47	0.93	3000	constant

Table 2 Properties of structural steel

Type	t (mm)	Yield stress (N/mm ²)	Ultimate strength (N/mm ²)	Elastic modulus (N/mm ²)	Poisson's ratio
Steel plate	2.7	349.7	516.1	204,033	0.28
Steel tube	5.7	405.8	451.3	200,450	0.30

Table 3 Main measured indexes of specimens

No.	P_y^* kN	Δ_y mm	P_{max} kN	Δ_{max} mm	P_u kN	Δ_u mm	μ -
CSW-T-1	4944	0.93	6499	1.89	5524	5.27	5.67
CSW-T-2	5444	0.78	6429	1.47	5463	4.68	6.01
CSW-T-3	5777	1.32	6416	2.05	5454	5.48	4.15
CSW-T-4	5044	1.57	5930	2.66	5041	4.81	3.06
CSW-T-5	5373	1.66	6042	2.23	5136	4.62	2.78
CSW-T-6	5376	1.87	5906	2.97	5020	5.52	2.95

* P_y is the yielding strength; Δ_y is the displacement corresponding to the P_y ; P_{max} is the axial strength; Δ_{max} is the displacement corresponding to the P_{max} ; P_u is 85% of the compressive strength in the descend branch; Δ_u is the displacement corresponding to the P_u ; μ is the ductility.

Table 4 Main measured indexes of specimens

No.	Loading direction	P_y	Δ_y	Δ_y/h_w^a	P_{max}	Δ_{max}	Δ_{max}/h_w^a	P_u	Δ_u	Δ_u/h_w^a	μ
		kN	mm	-	kN	mm	-	kN	mm	-	-
CSW-T-03	(+)	416	5.7	1/141	509	13.5	1/59	468	17.3	1/46	3.05
	(-)	382	4.8	1/167	473	8.6	1/93	402	23.4	1/34	4.88
CSW-T-05	(+)	433	5.0	1/160	515	9.3	1/86	438	12.1	1/66	2.42
	(-)	518	5.3	1/151	658	10.7	1/75	567	13.2	1/61	2.49

Table 5 Main measured indexes of specimens CSW-T-1 to CSW-T-6

No.	P_{max}	P_{EC4}	P_{max}/P_{EC4}	P_{CECS}	P_{max}/P_{CECS}	P_{AISC}	P_{max}/P_{AISC}
	kN	kN		kN		kN	
CSW-T-1	6499	5029	1.29	4924	1.32	4614	1.41
CSW-T-2	6429	5029	1.28	4924	1.31	4614	1.39
CSW-T-3	6416	5029	1.28	4924	1.30	4614	1.39
CSW-T-4	5930	5029	1.18	4924	1.20	4614	1.29
CSW-T-5	6042	5029	1.20	4924	1.23	4614	1.31
CSW-T-6	5906	5029	1.17	4924	1.20	4614	1.28